

Battery-like Supercapacitors from Vertically Aligned Carbon Nanofiber Coated Diamond: Design and Demonstrator

Siyu Yu, Nianjun Yang,* Michael Vogel, Soumen Mandal, Oliver A. Williams, Siyu Jiang, Holger Schönherr, Bing Yang, and Xin Jiang*

To fabricate battery-like supercapacitors with high power and energy densities, big capacitances, as well as long-term capacitance retention, vertically aligned carbon nanofibers (CNFs) grown on boron doped diamond (BDD) films are employed as the capacitor electrodes. They possess large surface areas, high conductivity, high stability, and importantly are free of binder. The large surface areas result from their porous structures. The containment of graphene layers and copper metal catalysts inside CNFs leads to their high conductivity. Both electrical double layer capacitors (EDLCs) in inert solutions and pseudocapacitors (PCs) using $\text{Fe}(\text{CN})_6^{3-/4-}$ redox-active electrolytes are constructed with three- and two-electrode systems. The assembled two-electrode symmetrical supercapacitor devices exhibit capacitances of 30 and 48 mF cm^{-2} at 10 mV s^{-1} for EDLC and PC devices, respectively. They remain constant even after 10 000 charging/discharging cycles. The power densities are 27.3 and 25.3 kW kg^{-1} for EDLC and PC devices, together with their energy densities of 22.9 and 44.1 W h kg^{-1} , respectively. The performance of these devices is superior to most of the reported supercapacitors and batteries. Vertically aligned CNF/BDD hybrid films are thus useful to construct high-performance battery-like and industry-orientated supercapacitors for future power devices.

1. Introduction

Battery-like supercapacitors refer to those electrochemical capacitors (ECs) that possess the features of both ECs (e.g., high power density, P) and batteries (e.g., high energy density, E), as well as big capacitances (C) and long capacitance retention. These ECs meet the demands for powering future multifunctional electronics, hybrid electric vehicles, and industrial equipment.^[1] The construction of such battery-like supercapacitors is thus becoming the core activity of EC researches in recent years.

To fabricate battery-like supercapacitors, the first issue to be considered is the choice of suitable capacitor electrodes. Besides large surface areas, it is essential for them to facilitate high electron and ion mobilities. To produce capacitor electrodes with such properties, several strategies have been proposed^[2] by means of (1) improving the conductivity of the electrodes;

(2) employing nanosized electrode materials to reduce the diffusion length and meanwhile to enhance the surface areas; (3) utilizing 3D materials to realize ion diffusion in multiple directions (e.g., porous materials); and (4) reducing the diffusion activation energy of the ions. In these studies, various carbon materials with different hybridizations of atomic orbitals (sp^2 and sp^3), different allotropes of carbon (e.g., fullerenes, nanotubes, graphene, diamond, etc.), and various dimensionalities (e.g., 0D–3D) have been intensively investigated.^[3] For most ECs in these approaches, carbon materials have to be mixed with organic binders (e.g., polytetrafluoroethylene^[4]) and further pressed or coated on an electrode supporter (a current collector). Due to the low conductivity and relatively poor stability of these organic binders, both electron mobility inside the formed capacitor electrodes and ion diffusion on the surface of these capacitor electrodes are partially hindered. In most cases, the theoretically expected performance of the fabricated ECs has not been observed. Therefore, novel capacitor electrodes, namely binder-free carbon capacitor electrodes, are highly needed for the construction of battery-like supercapacitors.

The second crucial issue for the construction of battery-like supercapacitors is the selection of the electrolytes. For example, inert electrolytes are widely employed for the formation of electrical double layer capacitors (EDLCs). In these solutions, redox

S. Yu, Dr. N. Yang, Dr. M. Vogel, Prof. X. Jiang
Institute of Materials Engineering
University of Siegen
57076 Siegen, Germany
E-mail: nianjun.yang@uni-siegen.de; xin.jiang@uni-siegen.de

Dr. S. Mandal, Prof. O. A. Williams
School of Physics and Astronomy
Cardiff University
Cardiff CF24 3AA, UK

S. Jiang, Prof. H. Schönherr
Physical Chemistry I
Department of Chemistry and Biology and Research Center
of Micro and Nanochemistry and Engineering (Cμ)
University of Siegen
57076 Siegen, Germany

Dr. B. Yang
Shenyang National Laboratory for Materials Science
Institute of Metal Research (IMR)
Chinese Academy of Sciences (CAS)
No.72 Wenhua Road, Shenyang 110016, China

 The ORCID identification number(s) for the author(s) of this article can be found under <https://doi.org/10.1002/aenm.201702947>.

DOI: 10.1002/aenm.201702947

species coated conductive substrates with polymers and metal oxides are also employed as the capacitor electrodes to produce pseudocapacitors (PCs).^[5] An alternative, but more efficient approach to construct PCs is to introduce soluble redox species into the electrolyte.^[6] One of the main advantages of this novel approach is that the amount of redox species, which determines the charge storage capacity, is easy to be controlled. However, the contribution of soluble redox electrolytes to the performance of ECs has not been clearly clarified.^[7] Therefore, the development of battery-like supercapacitors in both inert and redox electrolytes should be conducted.

We are thus interested in the growth of a novel binder-free carbon capacitor electrode as well as its employment for the construction of battery-like supercapacitors, including EDLCs in inert electrolytes and PCs in redox electrolytes. The binder-free carbon capacitor electrode is constructed using boron doped diamond (BDD) as the electrode supporter and vertically aligned carbon nanofibers (CNFs) as the active electrode materials. The CNFs are directly grown on BDD with a thermal chemical vapor deposition (TCVD) process (Figure S1, Supporting Information). Namely, such a TCVD process eliminates the need to use low conductive organic binders. For such growth, C_2H_2 is employed as the reaction gas. The copper (Cu) thin film sputtered with a physical vapor deposition (PVD) device acts as the catalyst. Moreover, in this way, the CNFs are covalently bonded to BDD via stable C–C bonds, i.e., the CNFs on diamond exhibit good adhesion, increased conductivity, and long-term stability. Furthermore, the CNFs feature high electrical conductivity, large specific surface area, good chemical stability, and 3D porous structures.^[8] Abundant diffusion channels and plenty of active sites are thus expected to be available for our capacitor electrode. Therefore, the hybrid structure of CNF/BDD films will offer integrated properties of both carbon materials used and resolve the key bottlenecks for the construction of battery-like supercapacitors mentioned above.

In this contribution, we first present the details about the growth of vertically aligned CNFs on BDD, followed by the characterization of their morphology, chemical structure, and wettability using scanning electron microscopy (SEM), transmission electron microscopy (TEM), X-ray photoelectron spectroscopy (XPS), Raman, and water contact angle measurements. The construction of ECs with CNF/BDD hybrid films as the capacitor electrodes is then shown. Using both three- and two-electrode configurations, their performance is evaluated in the inert solution (1.0 M H_2SO_4) as well as in the redox species contained electrolyte (1.0 M Na_2SO_4 + 0.05 M $Fe(CN)_6^{3-/4-}$). At last, a stand-alone supercapacitor is demonstrated.

2. Results and Discussion

2.1. Design of CNF/BDD Capacitor Electrodes

A good capacitor electrode features high electrical conductivity, a large specific surface area, good chemical stability, and a 3D porous structure. CNFs grown on BDD are believed to be the potential candidates since it has been shown that in a TCVD technique, the growth (e.g., size, length, density) of CNFs is actually determined by the thickness of a catalyst (in our case,

the Cu film).^[9] To fabricate such a capacitor electrode, the growth of CNFs on BDD was first optimized. The SEM images of Cu films sputtered on BDD with different sputtering times ($t_{Cu,s}$) of 15, 30, 60, 90, and 120 s were thus recorded. Figure 1a shows one typical SEM image of a Cu film with $t_{Cu,s}$ of 60 s. The SEM images of Cu films with $t_{Cu,s}$ of 15, 30, 90, and 120 s are shown in Figure S2 (Supporting Information). In all these images, BDD films are fully covered with Cu. The thicknesses of Cu films vary from a dozen to tens of nanometers, increasing as a function of $t_{Cu,s}$. With $t_{Cu,s}$ from 15 to 90 s, the crystal boundaries of BDD can be clearly observed, but become indistinct once $t_{Cu,s}$ is up to 120 s. These Cu films were then applied as the catalyst for the growth of CNFs. The surface morphologies of as-grown CNF/BDD hybrid films were then

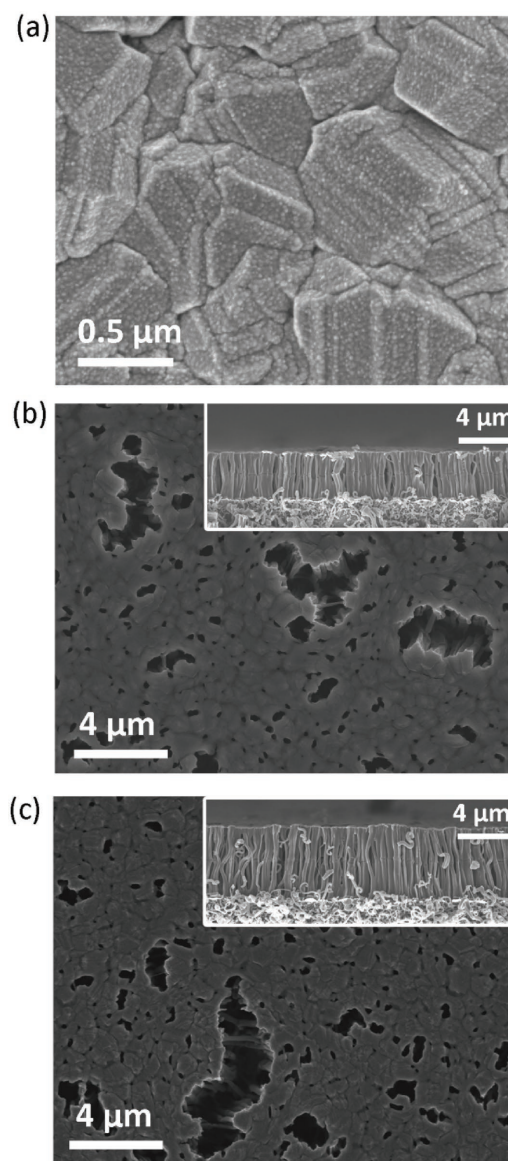


Figure 1. Characterization: SEM images of a) a Cu film on BDD, b) a CNF film on BDD with a growth time of 60 min, c) a CNF film with a growth time of 90 min. The time for Cu sputtering was 60 s. The inset images show the cross-sections of as-grown CNFs.

checked using SEM. As an example, the SEM images in top and side views for $t_{\text{Cu,s}}$ of 60 s are shown in Figure 1b. Those for $t_{\text{Cu,s}}$ of 15, 30, 90, and 120 s are shown in Figure S3 (Supporting Information). For $t_{\text{Cu,s}}$ of 15 s, the growth of CNFs is random. While, CNFs are quasivertically aligned when $t_{\text{Cu,s}}$ is up to 30 s. When $t_{\text{Cu,s}}$ is longer than 60 s, vertically aligned CNFs with much denser arrangement are acquired. The thicknesses of CNFs (insets in SEM images) are measured to be about 2.5, 2.8, 3.6, 4.3, and 5.0 μm for $t_{\text{Cu,s}}$ of 15, 30, 60, 90, and 120 s, respectively. Interestingly, all CNF films exhibit 3D porous properties. Lots of channels or pores exist between CNFs, even for the CNFs with $t_{\text{Cu,s}}$ longer than 60 s. This is partially because the growth direction of CNFs is perpendicular to the substrate. The surface morphology of CNF films is closely dependent on that of the substrate. For instance, the surface characteristic of the CNF film for $t_{\text{Cu,s}}$ of 60 s (Figure 1b) shows actually the morphology of BDD surface. At some irregular crystal boundaries of BDD, tilted CNFs are then obtained and pores are generated. Such a statement is further supported by the control experiments using a smooth Si substrate as the supporter for the growth of CNFs. In this case, only a smooth surface of the CNF films was obtained under identified conditions (Figure S4, Supporting Information).

To figure out the effect of the morphology of Cu catalysts on the growth of CNFs on BDD, the growth of CNFs using Cu particles as catalyst was further tested. These Cu particles were generated via annealing the Cu films at 500 $^{\circ}\text{C}$ for 60 min (Figure S5, Supporting Information). Vertically aligned CNFs are gained with $t_{\text{Cu,s}}$ of 90 and 120 s (Figure S6, Supporting Information). Interestingly, the thicknesses of CNF films are slightly smaller than those CNF films obtained without annealing (WOA) of the Cu films. More details can be found in the “Experimental” section of the Supporting Information. Therefore, the copper films WOA were used throughout our studies.

Obviously, altering the growth time leads to the formation of CNFs with various lengths. In a case study, Cu films sputtered with $t_{\text{Cu,s}}$ of 60 s WOA were applied for the growth of CNFs using different growth times. The SEM images of CNFs grown using growth times of 60, 90, 30, and 120 min are shown in Figure 1b,c and Figure S7a,b (Supporting Information), respectively. As expected, the surface morphologies of these CNF/BDD hybrid films are almost identical. The lengths of CNFs are about 1.8, 3.6, 5.5, and 7.2–8.0 μm for growth times of 30, 60, 90, and 120 min, respectively. Consequently, much longer CNFs are possible to be attained once a longer growth time (e.g., > 120 min) is applied or a higher C_2H_2 concentration (e.g., > 500 mbar) is used.

Prior to employing CNF/BDD hybrid films as the capacitor electrodes, their wettability was checked. The as-grown CNF/BDD hybrid films were not water-wettable. This is the characteristic of the CNFs. These CNFs were then wet-chemically treated via immersing them in a mixture of H_2SO_4 and HNO_3 ($v/v = 3:1$) for 30 min. As a case study, the wettability of CNFs with $t_{\text{Cu,s}}$ of 60 s WOA (Figure 1b) was examined. The detected static contact angle of water on the as-grown CNFs is $110.4^{\circ} \pm 1.0^{\circ}$ (Figure S8a, Supporting Information), revealing its hydrophobic nature. Its XPS survey spectrum (Figure S8c, Supporting Information) exhibits the C 1s (98.1 at%) and

O 1s (1.9 at%) signals at 284.0 and 532.0 eV, respectively. After such a wet-chemical treatment, the contact angle of water on the treated CNFs surface is changed to $24.0^{\circ} \pm 0.6^{\circ}$ (Figure S8b, Supporting Information). Accordingly, the oxygen content estimated from its XPS survey spectrum rises to 11.6 at% (Figure S8d, Supporting Information). Therefore, the wet-chemical treatment enhances the content of oxygen on the surface of CNFs. The enhanced degree of the hydrophilic terminations then leads to significantly improved wettability of CNF/BDD hybrid films in aqueous solution. Such a wet-chemical treatment was then always applied for the CNFs used for electrochemical experiments.

To optimize the CNF/BDD hybrid films for the later construction of both EDLCs and PCs, cyclic voltammograms (CVs) of different CNF/BDD hybrid films were recorded in 1.0 M H_2SO_4 at a scan rate of 100 mV s^{-1} . For the growth of these films, $t_{\text{Cu,s}}$ was varied from 15 to 120 s. Within investigated CNF/BDD hybrid films, half of them were grown using annealed copper films (WA) as the catalysts, the rest were grown using those copper films WOA as the catalysts. The growth time for these CNFs was 60 min. For these tests, a three-electrode system was used. Figure S9a (Supporting Information) shows two typical CVs for CNF/BDD WA and WOA films with $t_{\text{Cu,s}}$ of 60 s. At the same potential, the capacitive current of the CNF/BDD hybrid film WOA is larger, an indication of a higher capacitance. Figure S9b (Supporting Information) summarizes the calculated capacitances of all the CNF/BDD hybrid films as a function of $t_{\text{Cu,s}}$. These capacitances were estimated from their correspondent CVs. In the case of CNF/BDD hybrid films WA, almost no variation of capacitances is observed when different $t_{\text{Cu,s}}$ are applied. The nearly unchanged capacitances suggest the constant electrode areas of these CNFs. By using CNF/BDD hybrid films WOA, the magnitude of the capacitance improves with an increase of $t_{\text{Cu,s}}$ up to 60 s and then remains almost constant until 90 s. On the contrary, a further increase of $t_{\text{Cu,s}}$ longer than 90 s leads to a decrease of the magnitude of the capacitance. Again, the change of the capacitance reflects directly the variation of surface areas of the formed CNF/BDD hybrid films WOA. For $t_{\text{Cu,s}}$ in the range from 60 to 90 s, the highest capacitance (about 36 mF cm^{-2}) is achieved. For further capacitance investigation, CNF/BDD hybrid films WOA grown with a relatively shorter copper sputter time (e.g., $t_{\text{Cu,s}} = 60$ s) were chosen as EC capacitor electrodes.

To reveal the structures of these CNFs, they were further examined with TEM and Raman. Figure 2a shows one representative TEM image of a CNF, whose lateral size is about 200 nm. The black triangle inside the CNF is a Cu catalyst. Its selected area electron diffraction (SAED) pattern of the [110] zone axis is shown in the inset of Figure 2a, proving good crystallinity of a Cu catalyst. Figure 2b shows the high magnification of the interface between a Cu catalyst and a CNF, where graphite is formed around the Cu catalyst. Lattice fringes with a distance of about 0.34 nm of the CNF are seen from the high resolution TEM (HRTEM) image of Figure 2c, confirming the formation of graphene-like layers around the Cu catalyst.^[10] In the region far away the Cu catalyst, the characteristics of amorphous carbon are detected, based on the HRTEM image and the fast Fourier transformation (FFT) image shown in Figure 2d. In addition, observation of a large number of the

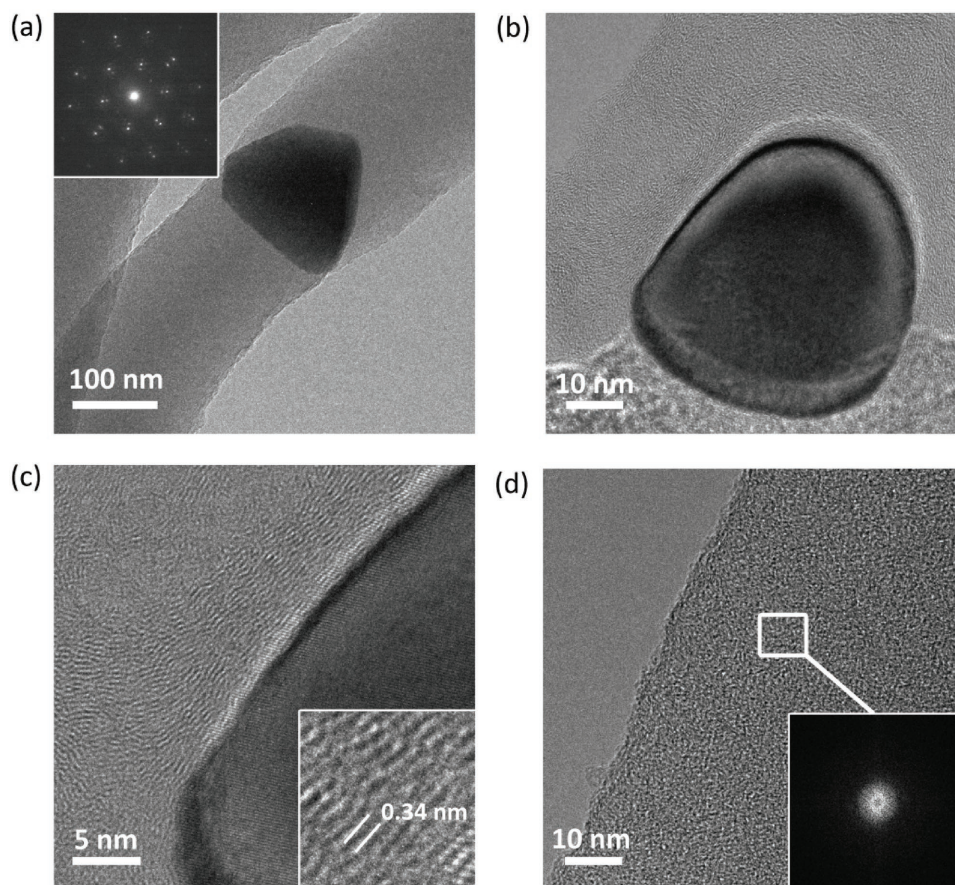


Figure 2. Characterisation, a) TEM image of a CNF with a Cu catalyst. The inset shows the SAED pattern of the Cu catalyst. b) TEM image of the interface between a CNF and a Cu catalyst. c) High-magnification TEM image of (b). The inset reveals the lattice fringes of graphite. d) HRTEM and FFT (inset) images of the amorphous phase in the CNF.

CNFs confirms that graphitization only occurs in the region around the Cu catalyst.

A Raman spectrum of the CNF/BDD hybrid film (Figure S10, Supporting Information) reveals two major Raman bands: D band at $\approx 1370\text{ cm}^{-1}$ and G band at $\approx 1650\text{ cm}^{-1}$. The D band is attributed to the disordered structure or defects of graphitic sheets. The broad peak observed at around 2800 cm^{-1} is probably related to the 2D band of graphite layers. Furthermore, the G band indicates the crystalline graphitic structure.^[11] The ratio of the intensity of the G band (I_G) to that of D band (I_D) is known to be proportional to the graphitization degree of carbon materials. In our case, the value of I_G/I_D , calculated using Gaussian fitting of two peaks, is about 0.42, confirming the large amount of amorphous phases and relatively few graphitic crystallites in the CNFs.^[10]

The existence of graphite and Cu inside the CNFs improves the electrical conductivity of the formed material. A more detailed study of the conductivity using scanning tunneling microscope is still under investigation. Together with their large surface area and a porous structure, CNF/BDD hybrid films with $t_{\text{Cu,s}}$ of 60 s WOA are expected to facilitate ion transfer in the solution and electron mobility on the interface of a CNF/BDD electrode.

2.2. Performance of CNF/BDD ECs

2.2.1. Capacitance

The CNF/BDD hybrid film with $t_{\text{Cu,s}}$ of 60 s WOA was employed as the capacitor electrode to fabricate ECs. Its capacitances were first studied using a three-electrode system. For the construction of EDLCs, its CVs in $1.0\text{ M H}_2\text{SO}_4$ were recorded within the potential range of 0–1.0 V at different scan rates (Figure S11a, Supporting Information). The CVs are nearly rectangular, indicating ideal EDLC behavior. The slight deviation of the CVs from rectangular shape is due to the altered charge transfer resistance (R_{ct}) between CNF pores and electrolyte interfaces as well as a generated overpotential.^[12] The estimated capacitances are 36.4, 48.2, 80.1, and 116.3 mF cm^{-2} at the scan rates of 100, 50, 20, and 10 mV s^{-1} , respectively. Figure S11b (Supporting Information) presents the galvanostatic charging/discharging (GCD) curves at current densities ranging from 2 to 20 mA cm^{-2} . At high current densities, the curves are almost symmetrical, demonstrating high reversibility of this EDLC. The IR drop observed at the scan rate of 2 mA cm^{-2} is probably due to the internal resistance of CNF films and R_{ct} caused mainly by diffusion kinetics of the ions. The calculated capacitances are

17.6, 27.7, 56.6, and 137.9 mF cm⁻² at the current densities of 20, 10, 5, and 2 mA cm⁻², respectively.

The CNF/BDD PCs were then fabricated by introducing redox species (here 0.05 M Fe(CN)₆^{3-/4-}) into 1.0 M Na₂SO₄ aqueous solution. Figure S11c (Supporting Information) shows the CVs recorded in a potential window of -0.2–0.8 V at different scan rates. At all scan rates, the CV curves show a pair of redox waves corresponding to the redox reaction of [Fe(CN)₆]³⁻ + e⁻ ↔ [Fe(CN)₆]⁴⁻. The peak potential separation (ΔE_p) is relatively small (e.g., ΔE_p = 96 mV at a scan rate of 10 mV s⁻¹). Moreover, the anodic peak currents are identical to the absolute values of the cathodic ones, indicating the excellent reversibility of these PCs. The evaluated capacitances are 35.0, 52.5, 94.8, and 136.8 mF cm⁻² at the scan rates of 100, 50, 20, and 10 mV s⁻¹, respectively. The related GCD curves are shown in Figure S11d (Supporting Information). All these recorded curves show nonlinear behavior with plateaus, relating to redox reactions of Fe(CN)₆^{3-/4-}. The times for the charging and discharging processes are almost identical at all current densities, again demonstrating perfect reversibility of this PC. The estimated capacitances are 14.5, 34.7, 84.6, and 232.0 mF cm⁻² at the current densities of 20, 10, 5, and 2 mA cm⁻², respectively.

At high scan rates (e.g., 100 mV s⁻¹) and high current densities (e.g., 20 mA cm⁻²), the capacitances of a PC are slightly smaller than those of an EDLC. Besides two different charge storage mechanisms (namely charge accumulation for EDLCs, charge transfer and accumulation for PCs), there exist additional aspects. First, different supporting electrolytes are employed for these ECs. Namely, the supporting electrolyte used for PCs is Na₂SO₄, while for EDLCs, H₂SO₄ is applied as the electrolyte. To clarify the effect of these electrolytes, the CVs of an EDLC in 1.0 M H₂SO₄ and in 1.0 M Na₂SO₄ were recorded at the scan rate of 100 mV s⁻¹ (Figure S12, Supporting Information). The capacitive current obtained in 1.0 M Na₂SO₄ is much smaller, resulting in a low capacitance of 8.3 mF cm⁻². The difference can be interpreted as altered conductivity of the electrolytes. For the electrolyte of 1.0 M H₂SO₄, the conductivity is 1000 mS cm⁻¹. For the electrolyte of 1.0 M Na₂SO₄, it is only 80 mS cm⁻¹.^[13] Moreover, the size of Na⁺ ions in hydrated state is larger than that of hydrated protons. The mobility of Na⁺ ions in the solution is slower. Their accessibility and accumulation to the pores of the densely packed CNFs are thus hindered. If one compares the capacitance of the EDLC using Na₂SO₄ with that of a PC, the capacitance of a PC is enlarged for more than four times even at high scan rates (e.g., 100 mV s⁻¹). Such enhancement of the capacitance is similar or even better than those reported by using other porous carbon materials.^[14] Second, the inferior behavior of the PC at high scan rates or current densities can be attributed to kinetically unfavorable diffusion of ions inside the narrow pores because of slow Na⁺ ionic motion and low conductivity of the electrolyte, leading to loss of the full contribution of active surface area of a CNF film.

To figure out clearly the contribution of CNFs into the construction of these ECs, the capacitance of the fabricated EDLC is compared with that of reported EDLCs constructed using diamond nanostructures or hybrid films of BDD with carbon materials (Figure S13, Supporting Information). Clearly, BDD nanostructures (e.g., honeycomb diamond,^[15] porous diamond,^[16] diamond networks,^[17] etc.) own enhanced surface areas and

thus exhibit significantly improved capacitances in comparison to flat BDD films. The hybrid films of BDD with other carbon materials (e.g., carbon nanotube,^[18] carbon fiber,^[19] etc.) also deliver larger capacitances than BDD EDLCs. This is attributed partially to further increased surface areas, partially to the addition of the capacitances from other carbon materials. Compared with these values, the capacitance of CNF/BDD EDLC in this study is the highest. Moreover, the comparison of the capacitances of different diamond PCs is shown in Figure S13 (Supporting Information). The capacitance of the CNF/BDD PC reaches the highest value of 232.0 mF cm⁻². It is much larger than that of metal oxide (e.g., Ni(OH)₂^[20]), conducting polymer (e.g., poly(3,4-(ethylenedioxy)thiophene (PEDOT)^[21]), and diamond nanowire-based PCs. It is also higher than that when a diamond network was utilized as the capacitor electrode and the redox solution was the electrolyte.^[17a] In summary, the large surface area, the improved electrical conductivity, and the unique porous structure of these vertically aligned CNFs on BDD lead to the high performance of these EDLCs and PCs.

The effect of the growth time of CNFs on the capacitances of CNF/BDD hybrid films were also examined in 1.0 M H₂SO₄ using a three-electrode system. The CVs of CNFs with growth times of 30, 90, and 120 min were recorded at a scan rate of 100 mV s⁻¹ (Figure S14a, Supporting Information). The capacitances calculated from the related CVs are listed in Figure S14b (Supporting Information). The magnitude of the capacitance improves almost linearly with an increase of growth time of CNFs. This is because the lengths of CNFs, namely the surface area of a CNF film, are enhanced nearly linear as a function of the growth time. In other words, the capacitance of these CNF/BDD ECs is possible to be further improved as required only through applying longer TCVD growth times.

For practical applications of these ECs, a two-electrode symmetrical supercapacitor device was assembled. Two CNF/BDD hybrid films were used as the capacitor electrodes. These films were grown with t_{CNF} of 60 s WOA. The performance of as-fabricated ECs was first investigated in 1.0 M H₂SO₄ aqueous solution. Figure 3a shows the CV curves recorded at the scan rates of 100, 50, 20, and 10 mV s⁻¹ and with a cell voltage of 1.0 V. Similar as the results obtained by a three-electrode system, the CVs show nearly rectangular shape at low scan rates, revealing good double layer capacitive behavior. The calculated capacitances are 7.7, 11.7, 21.6, and 30.4 mF cm⁻² at the scan rates of 100, 50, 20, and 10 mV s⁻¹, respectively.

The related GCD curves of the EDLC device recorded at the current densities from 1 to 20 mA cm⁻² are presented in Figure 3b. The curves are almost symmetric at high current densities, demonstrating the high reversibility of the EC. When lower current densities (here smaller than 2 mA cm⁻²) are applied, asymmetrical curves are acquired, due to the charge transfer resistance at the electrode and electrolyte interfaces. The times required for charging and discharging processes are almost equivalent, indicating a high Coulombic efficiency of the EDLC. The calculated capacitances are 2.1, 4.0, 6.8, 19.6, and 34.0 mF cm⁻² at the current densities of 20, 10, 5, 2, and 1 mA cm⁻², respectively.

Considering that fast charging/discharging processes are required for ECs, CV measurements at high scan rates (e.g., up to 3 V s⁻¹) were carried out. The related CVs are displayed in Figure S15a (Supporting Information).

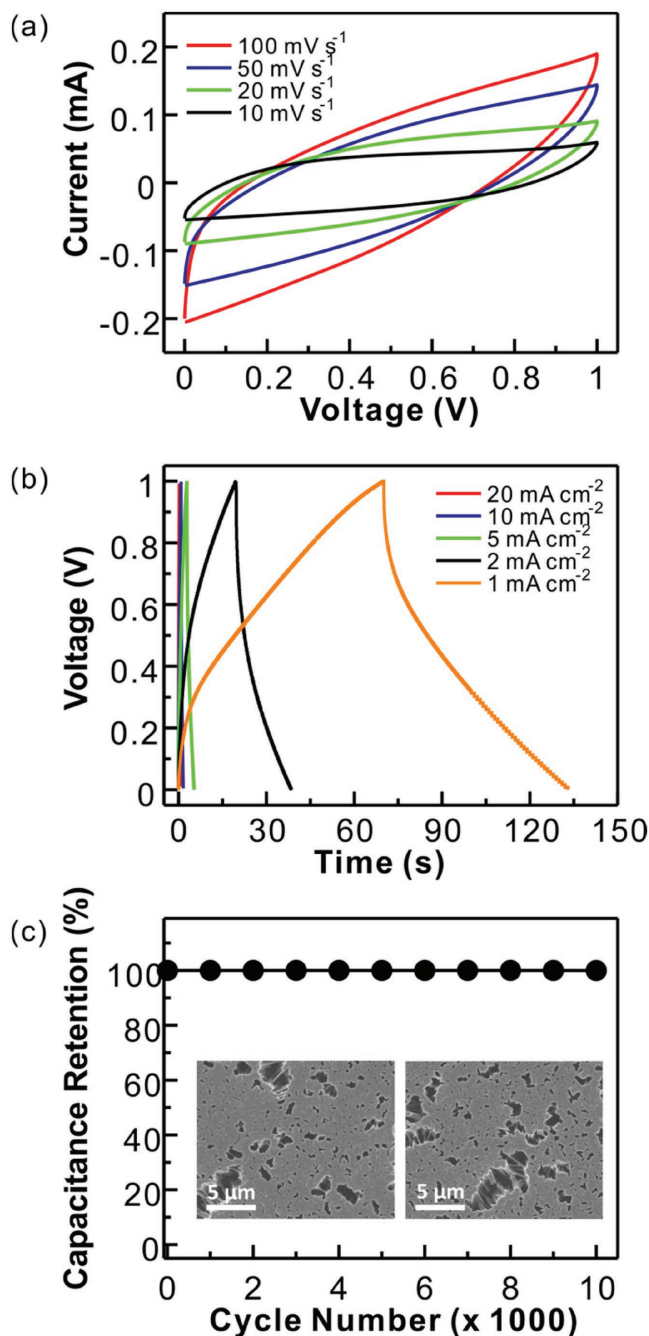


Figure 3. Performance of a CNF/BDD symmetric EDLC device in 1.0 M H₂SO₄, a) CVs recorded at the scan rates of 100, 50, 20, and 10 mV s⁻¹, b) charging/discharging curves at the current densities of 1, 2, 5, 10, and 20 mA cm⁻², c) capacitance retention at the charging/discharging current density of 5 mA cm⁻². The inset SEM images show the morphologies of two used CNF/BDD hybrid films after 10 000 charging/discharging cycles.

Deformation of the CV curves is noticed at these high scan rates. This is quite normal due to insufficient time for ion adsorption/desorption and diffusion into the inner pores. In this context, the capacitance decreases with an increase of the scan rate, as shown in Figure S15b (Supporting Information). Consequently, these CNF/BDD EDLCs are possible to be applied for fast charging/discharging processes.

On the other hand, the capacitance of a PC device was then evaluated in a cell voltage of -0.5–0.5 V in 1.0 M Na₂SO₄ solution containing 0.05 M Fe(CN)₆^{3-/4-}. At all scan rates, the CV curves (Figure 4a) show a pair of well-defined peaks, relating to the redox reaction of Fe(CN)₆^{3-/4-}. In addition, the integrated charges from the anodic and cathodic cycles evidence that the charges

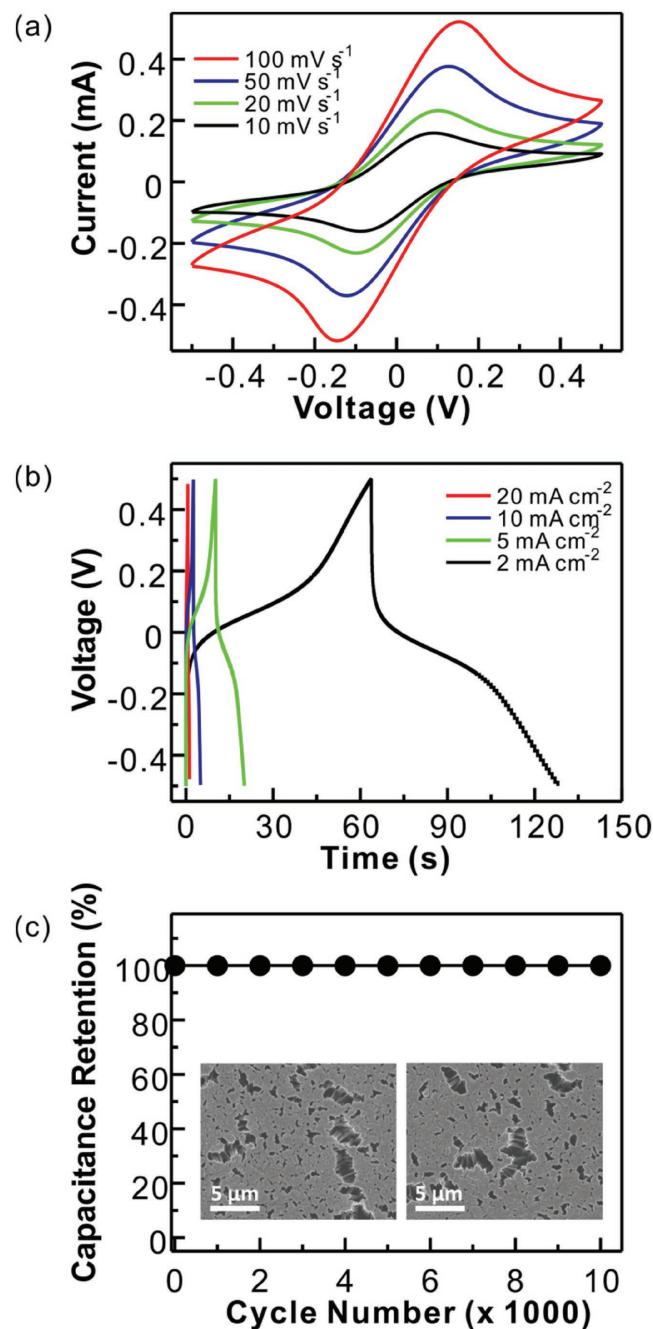


Figure 4. Performance of a CNF/BDD symmetric PC device in 0.05 M Fe(CN)₆^{3-/4-} + 1.0 M Na₂SO₄, a) CVs at the scan rates of 100, 50, 20, and 10 mV s⁻¹, b) charging/discharging curves at the current densities of 2, 5, 10, and 20 mA cm⁻², c) capacitance retention at the charging/discharging current density of 10 mA cm⁻². The inset SEM images show the surface characteristics of two used CNF/BDD hybrid films after 10 000 charging/discharging cycles.

stored on the electrodes during a charging process are nearly identical to those removed during a discharging process. The calculated capacitances are 15.7, 23.3, 36.1, and 48.1 mF cm⁻² at the scan rates of 100, 50, 20, and 10 mV s⁻¹, respectively.

Figure 4b presents the GCD curves of this PC device at different charging/discharging current densities. The plateaus in the curves are relative to the redox reactions of Fe(CN)₆^{3-/4-}. Almost same times are required for charging and discharging processes even at a low current density of 2 mA cm⁻². The estimated Coulombic efficiency is about 100%, confirming the excellent reversibility of such a PC device. The calculated capacitances are 6.4, 12.8, 25.6, and 65.4 mF cm⁻² at the current densities of 20, 10, 5, and 2 mA cm⁻², respectively.

Interestingly, the capacitance of a PC device is several times larger in comparison to that of an EDLC device. Such an enlarged capacitance is the sum of both electrical double layer capacitance and pseudocapacitance. The former results from the charge/ion accumulation on the surface of CNF/BDD films. The latter originates from the rapid occurrence of Faradaic reaction of [Fe(CN)₆]³⁻ + e⁻ ↔ [Fe(CN)₆]⁴⁻ on the CNF/BDD interfaces. Moreover, when soluble redox species of Fe(CN)₆^{3-/4-} are added in the electrolyte, the charge-transfer resistance at the CNF/BDD interfaces is expected to be reduced, but the ionic conductivity of the solution is expected to be enhanced. These results are similar with those obtained on diamond networks.^[17a] This pseudocapacitance is thus much higher than that of the electrical double layer capacitance. In short, both the fabricated CNF/BDD EDLC and PC devices feature the characteristics of battery-like supercapacitors, in this case a large capacitance.

2.2.2. Capacitance Retention

The cycling stability of a CNF/BDD EDLC device was further examined using GCD technique at the current density of 5 mA cm⁻². After 10 000 cycles, the capacitance remains unchanged (Figure 3c). The morphologies of both the capacitor electrodes were then checked after the lifetime test. Their SEM images are shown in the insets of Figure 3c. In comparison to that of as-grown CNF films shown in Figure 1b, neither obvious surface damages nor differences regarding surface morphology or porosity are observed, demonstrating the excellent stability of the CNF/BDD capacitor electrode.

For the cycling stability test of a CNF/BDD PC device, a long time charging/discharging process (e.g., for 10 000 cycles) was carried out using GCD technique at the current density of 10 mA cm⁻². The capacitance retention as a function of the cycle number is shown in Figure 4c, illustrating that the initial capacitance remains unchanged after the lifetime test. The surface morphologies of two electrodes (the inset of Figure 4c) show almost no change, compared to the as-grown CNF films (Figure 1b), again demonstrating the perfect stability of the electrodes and also a high degree of the reversibility in the electrolyte.

Therefore, the CNF/BDD-based EDLC and PC devices have long-term cycle ability, one of the important advantages of battery-like supercapacitors.

2.2.3. Energy and Power Densities

To clarify the overall performance of the CNF/BDD EC devices, their energy and power densities were further calculated. The related Ragone plots are displayed in Figure 5. The estimated maximal *E* and *P* reach the values of 22.9 W h kg⁻¹ and 27.3 kW kg⁻¹ for an EDLC device, respectively. While for a PC device, they are 44.1 W h kg⁻¹ and 25.3 kW kg⁻¹, respectively. Compared to other energy devices (e.g., ECs, batteries, etc.^[22]) shown in Figure 5, the proposed CNF/BDD EC devices exhibit not only much higher *P*, but also higher *E* than those of some reported supercapacitors. The value of *E* is similar to that of batteries. The reason is ascribed to the structure of the electrodes and also the “battery-like” behavior of the Fe(CN)₆^{3-/4-} redox electrolyte.^[17a]

Table S1 (Supporting Information) further compares the performance (e.g., *E* and *P*) of our CNF/BDD EC devices with that of other CNF-based EC devices reported in the literature. The *E* and *P* values of our CNF/BDD EC devices are higher than those of many reported CNF-based EC devices.^[23] For instance, porous CNF-based EDLC devices only show an *E* of 17 W h kg⁻¹ and a *P* of 20 kW kg⁻¹.^[24] The *E* and *P* of EDLC devices fabricated by N,P-codoped CNF networks reach the values of 7.8 W h kg⁻¹ and 26.6 kW kg⁻¹, respectively.^[25] By applying V₂O₅/CNF composites as electrode material, the PC devices exhibit an *E* of 18.8 W h kg⁻¹, as well as a *P* of 20.0 kW kg⁻¹.^[26]

In conclusion, both the EDLC and PC devices fabricated from the CNF/BDD capacitor electrodes exhibit high power densities and high energy densities. They are characteristic for battery-like supercapacitors. Together with obtained large capacitances, long-term capacitance retention, battery-like EDLCs and PCs are successfully formed using vertically aligned carbon nanofibers grown on BDD as the capacitor electrodes.

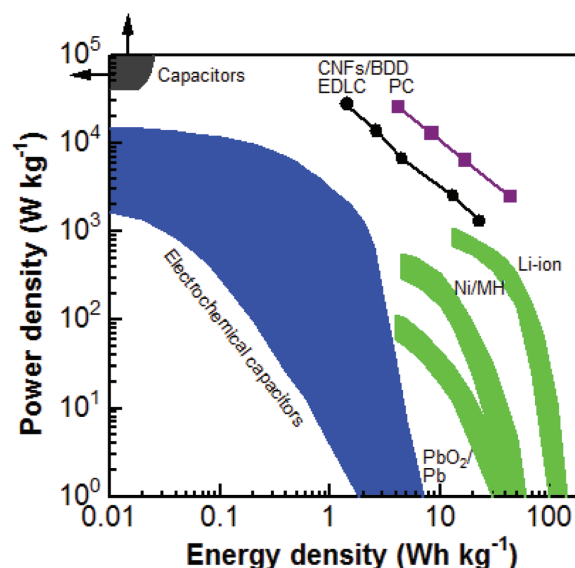


Figure 5. Performance of CNF/BDD EC devices in both inert solution and redox electrolyte: Ragone plots of CNF/BDD EDLCs (closed dots) and PCs (closed squares) in comparison with those^[22] of traditional capacitors, ECs, and batteries. Reproduced with permission.^[22] Copyright 2008, Macmillan Publishers Limited.

2.2.4. Battery-like Supercapacitor Demonstrator

A stand-alone and portable system was designed to demonstrate the proposed CNF/BDD ECs for practical applications. The built demonstrator (Figure 6a) consists of three EDLC devices assembled in series, a single-board microcontroller to control the charging/discharging processes, a red light-emitting diode (LED) (working voltage: 1.8 V), and a universal serial bus (USB) cable to charge this device. The designed prototype of a CNF/BDD EC device is schematically illustrated in Figure 6b. Two CNF/BDD capacitor electrodes are attached tightly to both sides of the cell, made from transparent acrylic glass. The efficient area of each electrode exposed to the electrolyte is about 0.785 cm². A 50 μ m Nafion membrane is fixed with two sheets in the middle of the cell. As a case study, the electrolyte (1.0 M H₂SO₄) was filled in the cell from the top.

Figure 6c shows the electrical circuit diagram of such a demonstrator. In the first step, the switch “1” is closed, the devices are charged by an external power supplier with the USB connector. The resistance in the circuit is used to adjust the charging current, or charging duration. When the measured voltage of the EC devices is up to 3 V, the switch “1” opens and then the switch “2” is closed, leading to powering and illuminating a commercial red LED. Moreover, the discharge process of the EC devices is possible to be tested. When the voltage is lower than 1.6 V, the switch “2” opens and the switch “1” is closed, and the EC devices are charged again. Such a process is automatically controlled by a single-board microcontroller. In other words, such ECs are also possible to be charged by

connecting to a computer or a power supplier with the USB connector (Figure 6a). Figure 6d shows the variation of voltages in the recorded curves during the charging/discharging processes as a function of time. The good repeatability of the curves reveals the excellent reversibility and stability of the device. With a charge time of about 70 s, the red LED lights up (Figure 6d). The light intensity is varied as a function of the applied voltages (the insets in Figure 6d). With a high voltage at an initial stage, the LED is very bright, indicating the capacitor features of ECs. The light lasts for few seconds and becomes weaker till it ceases. Therefore, the fabricated battery-like supercapacitors made from CNF/BDD hybrid films are promising for the employment of practical energy storage applications.

3. Conclusion

Vertically aligned carbon nanofibers directly grown on BDD, novel hybrid carbon materials, have been utilized as the capacitor electrodes to develop supercapacitors. Both electrical double layer capacitors using inert solutions and pseudocapacitors using redox electrolytes have been fabricated. These ECs feature large capacitance (in the range of mF cm⁻²), long-term capacitance retention, high power densities, and high energy densities. Such high energy and power densities achieved from the CNF/BDD EC devices are superior to those of reported batteries and supercapacitors. The high performance of these battery-like ECs is attributed to the large surface areas, improved electrical conductivity, and porous structures of these binder-free

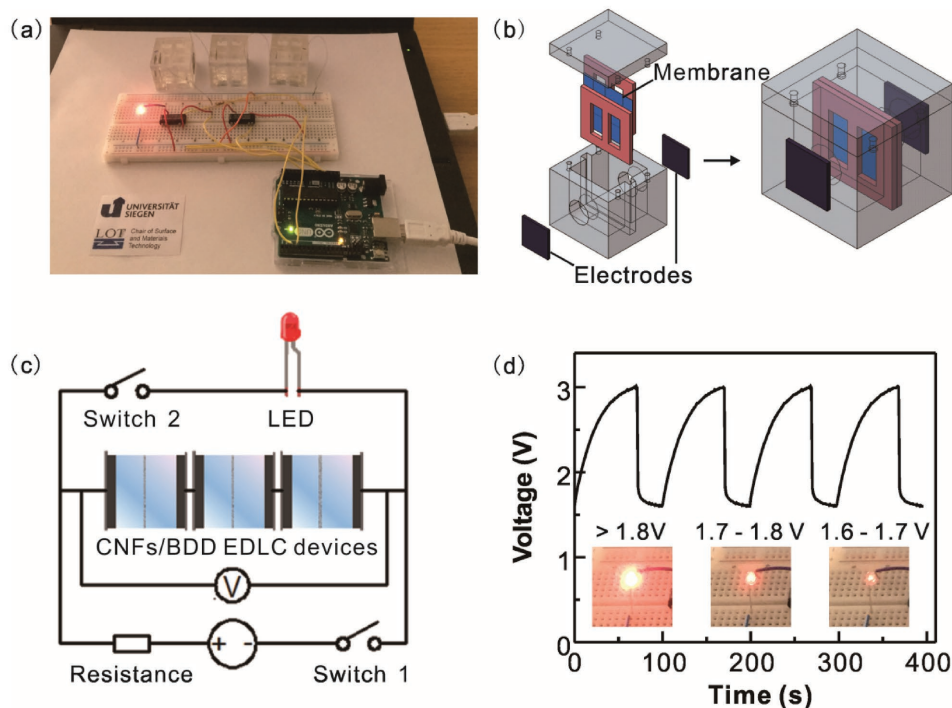


Figure 6. A stand-alone CNF/BDD EC demonstrator, a) A photograph of the demonstrator consisting of three CNF/BDD EDLC devices in series, a single-board microcontroller connected to the computer with a USB cable, and a red LED, b) the design of a CNF/BDD EC prototype used in the system, c) the schematic electrical circuit diagram related to (a), d) typical curves of the voltage as a function of time during the charging/discharging processes. The insets show the variation of light intensity of the red LED in relation to the cell voltage.

CNF/BDD hybrid films. Their performance is possible to be further enhanced only with longer CNFs (e.g., simply by applying a longer growth time). Future research activities can be focused on the employment of water-soluble but multielectron transferred redox electrolyte (e.g., heteropolyacids) as well as ionic redox electrolytes for the construction of battery-like supercapacitors. By use of these redox electrolytes, the improved performance of battery-like capacitors is expected, including their capacitances, capacitance retention, as well as power and energy densities. Moreover, these battery-like supercapacitors should be constructed at the large scales on the flexible substrates (e.g., carbon clothes). Together with the stand-alone demonstrator, the battery-like supercapacitors will be promising and possible for powering future multifunctional electronics, hybrid electric vehicles, and industrial equipment in the near future.

4. Experimental Section

Electrode Materials: Figure S1 (Supporting Information) illustrates schematically the steps for the growth of CNF/BDD hybrid films using a TCVD technique. First, BDD films were grown on silicon wafers using microwave plasma assisted chemical vapor deposition technique.^[27] Then, the coating of BDD with copper films was carried out on a PVD device. A high purity (99.999%) copper disk (4 in. in diameter) was used as the source material. The radio frequency (RF) magnetron sputtering tool was equipped with a turbo molecular pump and its base pressure was lower than 5×10^{-6} mbar. Prior to coating, a presputtering of the target for 10 min with a closed shutter was applied to clean the target. Applied coating conditions were: the substrate at room temperature, argon atmosphere, an argon gas flow of 50 sccm, a pressure of $3.5\text{--}4.5 \times 10^{-3}$ mbar. The thickness of copper films on BDD was varied through altering $t_{\text{Cu,s}}$. In this study, $t_{\text{Cu,s}}$ was varied from 15, 30, 60, 90 to 120 s. After that, copper coated BDD films were introduced in the center of a quartz tube in a TCVD device. To grow CNFs, these sputtered copper films were utilized as the catalysts. At a pressure of about 5×10^{-2} mbar, the tube was heated to 250 °C with a heating rate of 5 °C min⁻¹. Subsequently, the reaction gas of C₂H₂ was filled into the tube till a pressure of 500 mbar was reached. The growth times were varied from few minutes to few hours. After the growth, the reactor was rapidly evacuated. Once the pressure in the tube was lower than 5×10^{-2} mbar, the carbonization of CNFs was carried out. The carbonization temperature was 800 °C and the time applied was 60 min. As control experiments, copper films were annealed before the growth of CNFs in the TCVD device under the conditions of an annealing temperature of 500 °C, a pressure of about 5×10^{-2} mbar, and an annealing time for 60 min. To change the wettability of CNF/BDD hybrid films, they were immersed in a mixture of H₂SO₄ and HNO₃ (v/v = 3:1) for 30 min, then cleaned with deionized water, and finally dried in a N₂ atmosphere before the electrochemical experiments.

Characterization: The surface and cross-section morphologies of CNF/BDD hybrid films were investigated with field emission scanning electron microscopy (Zeiss Ultra55, Germany). The Raman spectra of these films were recorded on a homemade micro-Raman configuration with a 532 nm laser. An XPS (Surface Science Instruments, SSX-100 S-probe photoelectron spectrometer, USA) with an Al K α radiation of 200 W was used to characterize the elemental composition of these films. Static contact angle measurements were carried out on an OCA 15plus instrument (Data Physics Instruments GmbH, Filderstadt, Germany) with Milli-Q water drawn from a Millipore Direct Q8 system (Millipore, Schwalbach, with Millimark Express 40 filter, Merck, Germany) with a resistivity of 18.0 M Ω cm. The nanostructure of CNFs was further examined with TEM (FEI Tecnai G2 F30, USA). CNFs were collected via mechanical scratching from the BDD and then dispersed in ethanol. Subsequently, the ethanol containing nanostructures were

dropped on a thin carbon film covered copper grid using a drip pipe. After drying, the copper grid was examined under TEM.

Electrochemical Measurements: Electrochemical measurements were conducted on a CHI660E Potentiostat/Galvanostat (Shanghai Chenhua Inc., China). A standard three-electrode cell was utilized, where a CNF/BDD hybrid film acted as the working electrode, an Ag/AgCl (3 M KCl) electrode as the reference electrode, and a coiled Pt wire as the counter electrode. In a two-electrode symmetrical supercapacitor device, two CNF/BDD hybrid films served as the capacitor electrodes and a 50 μ m thick Nafion film (Alfa Aesar) as the separator. The geometric area of a CNF/BDD hybrid capacitor electrode was 0.05 cm². For EDLCs, the electrolyte was 1.0 M H₂SO₄. For PCs, the electrolyte was 1.0 M Na₂SO₄ containing 0.05 M K₃Fe(CN)₆/K₄Fe(CN)₆. The CVs were recorded at the scan rates ranging from 10 to 100 mV s⁻¹. The GCD curves for EDLCs and PCs were obtained at different current densities. The specific capacitances (C, F cm⁻²), energy densities (E, W h kg⁻¹), and power densities (P, W kg⁻¹) of ECs were calculated according to the reported methods.^[17a,28]

Supporting Information

Supporting Information is available from the Wiley Online Library or from the author.

Acknowledgements

S.Y. gratefully acknowledges the financial support from the China Scholarship Council (Chinese Government Scholarship, Award no. 201408080015). S.Y. acknowledges Dr. Rainer Bornemann from University of Siegen for his valuable suggestions regarding the construction of the supercapacitor demonstrator. N.Y. acknowledges the financial support from the German Research Foundation (DFG) under project YA344/1-1. H.S. acknowledges the financial support from the European Research Council (ERC project ASMI DIAS, Grant no. 279202) and the University of Siegen.

Conflict of Interest

The authors declare no conflict of interest.

Keywords

battery-like supercapacitors, demonstrators, diamonds, supercapacitor performance, vertically aligned carbon nanofibers

Received: October 23, 2017

Revised: November 16, 2017

Published online:

- [1] a) W. Zuo, R. Li, C. Zhou, Y. Li, J. Xia, J. Liu, *Adv. Sci.* **2017**, *4*, 1600539; b) T. Brousse, D. Bélanger, J. W. Long, *J. Electrochem. Soc.* **2015**, *162*, A5185; c) C. Costentin, T. R. Porter, J.-M. Savéant, *ACS Appl. Mater. Interfaces* **2017**, *9*, 8649.
- [2] a) P. F. Smith, K. J. Takeuchi, A. C. Marschillok, E. S. Takeuchi, *Acc. Chem. Res.* **2017**, *50*, 544; b) L.-F. Chen, Y. Lu, L. Yu, X. W. Lou, *Energy Environ. Sci.* **2017**, *10*, 1777; c) C. Zhu, T. Liu, F. Qian, T. Y.-J. Han, E. B. Duoss, J. D. Kuntz, C. M. Spadaccini, M. A. Worsley, Y. Li, *Nano Lett.* **2016**, *16*, 3448; d) L. Mai, H. Li,

- Y. Zhao, L. Xu, X. Xu, Y. Luo, Z. Zhang, W. Ke, C. Niu, Q. Zhang, *Sci. Rep.* **2013**, 3, 1718.
- [3] a) J. Liu, L. Zhang, H. B. Wu, J. Lin, Z. Shen, X. W. Lou, *Energy Environ. Sci.* **2014**, 7, 3709; b) E. Frackowiak, F. Béguin, *Carbon* **2001**, 39, 937.
- [4] W. Wu, L. Yang, S. Chen, Y. Shao, L. Jing, G. Zhao, H. Wei, *RSC Adv.* **2015**, 5, 91645.
- [5] Y. Wang, Y. Xia, *Adv. Mater.* **2013**, 25, 5336.
- [6] C. Zhong, Y. Deng, W. Hu, J. Qiao, L. Zhang, J. Zhang, *Chem. Soc. Rev.* **2015**, 44, 7484.
- [7] a) V. Augustyn, P. Simon, B. Dunn, *Energy Environ. Sci.* **2014**, 7, 1597; b) P. Simon, Y. Gogotsi, B. Dunn, *Science* **2014**, 343, 1210; c) A. C. Forse, J. M. Griffin, C. Merlet, J. Carretero-Gonzalez, A.-R. O. Raji, N. M. Trease, C. P. Grey, *Nat. Energy* **2017**, 2, 16216; d) C. Prehal, C. Koczwar, N. Jäckel, A. Schreiber, M. Burian, H. Amenitsch, M. A. Hartmann, V. Presser, O. Paris, *Nat. Energy* **2017**, 2, 16215.
- [8] a) Y. Ma, N. Yang, X. Jiang, in *Carbon Nanoparticles and Nanostructures* (Eds: N. Yang, X. Jiang, D.-W. Pang), Springer International Publishing, Switzerland **2016**, p. 47; b) Y. Gao, G. P. Pandey, J. Turner, C. R. Westgate, B. Sammakia, *Nanoscale Res. Lett.* **2012**, 7, 651.
- [9] a) X. Jiang, *Phys. Status Solidi A* **2014**, 211, 2679; b) J. H. Xia, X. Jiang, C. L. Jia, *Appl. Phys. Lett.* **2009**, 95, 223110.
- [10] Y. Ma, X. Sun, N. Yang, J. Xia, L. Zhang, X. Jiang, *Chem. - Eur. J.* **2015**, 21, 12370.
- [11] a) Q. Yong, E. Maik, S. Thorsten, J. Xin, *Nanotechnology* **2007**, 18, 345607; b) Y. Liu, J. Zhou, L. Chen, P. Zhang, W. Fu, H. Zhao, Y. Ma, X. Pan, Z. Zhang, W. Han, E. Xie, *ACS Appl. Mater. Interfaces* **2015**, 7, 23515.
- [12] L. Hu, W. Chen, X. Xie, N. Liu, Y. Yang, H. Wu, Y. Yao, M. Pasta, H. N. Alshareef, Y. Cui, *ACS Nano* **2011**, 5, 8904.
- [13] a) D. Jiménez-Cordero, F. Heras, M. A. Gilarranz, E. Raymundo-Piñero, *Carbon* **2014**, 71, 127; b) K. Torchała, K. Kierzek, J. Machnikowski, *Electrochim. Acta* **2012**, 86, 260; c) X. Zhang, X. Wang, L. Jiang, H. Wu, C. Wu, J. Su, *J. Power Sources* **2012**, 216, 290.
- [14] a) S. Roldán, C. Blanco, M. Granda, R. Menéndez, R. Santamaría, *Angew. Chem., Int. Ed.* **2011**, 50, 1699; b) S. Roldán, Z. González, C. Blanco, M. Granda, R. Menéndez, R. Santamaría, *Electrochim. Acta* **2011**, 56, 3401.
- [15] K. Honda, T. N. Rao, D. A. Tryk, A. Fujishima, M. Watanabe, K. Yasui, H. Masuda, *J. Electrochem. Soc.* **2001**, 148, A668.
- [16] V. Petrák, Z. Vlčková Živcová, H. Krýsová, O. Frank, A. Zukal, L. Klimša, J. Kopeček, A. Taylor, L. Kavan, V. Mortet, *Carbon* **2017**, 114, 457.
- [17] a) S. Yu, N. Yang, H. Zhuang, S. Mandal, O. A. Williams, B. Yang, N. Huang, X. Jiang, *J. Mater. Chem. A* **2017**, 5, 1778; b) H. Zhuang, N. Yang, H. Fu, L. Zhang, C. Wang, N. Huang, X. Jiang, *ACS Appl. Mater. Interfaces* **2015**, 7, 5384.
- [18] C. Hébert, J. P. Mazellier, E. Scorsone, M. Mermoux, P. Bergonzo, *Carbon* **2014**, 71, 27.
- [19] a) E. C. Almeida, A. F. Azevedo, M. R. Baldan, N. A. Braga, J. M. Rosolen, N. G. Ferreira, *Chem. Phys. Lett.* **2007**, 438, 47; b) E. C. Almeida, M. R. Baldan, J. M. Rosolen, N. G. Ferreira, *Diamond Relat. Mater.* **2008**, 17, 1529.
- [20] F. Gao, C. E. Nebel, *Phys. Status Solidi A* **2015**, 212, 2533.
- [21] D. Aradilla, F. Gao, G. L. Malandrakis, W. Müller-Sebert, P. Gentile, M. Boniface, D. Aldakov, B. Iliev, T. J. S. Schubert, C. E. Nebel, G. M. Bidan, *ACS Appl. Mater. Interfaces* **2016**, 8, 18069.
- [22] P. Simon, Y. Gogotsi, *Nat. Mater.* **2008**, 7, 845.
- [23] a) Z. Liu, D. Fu, F. Liu, G. Han, C. Liu, Y. Chang, Y. Xiao, M. Li, S. Li, *Carbon* **2014**, 70, 295; b) C. H. Kim, B.-H. Kim, *J. Power Sources* **2015**, 274, 512; c) C. Tran, V. Kalra, *J. Power Sources* **2013**, 235, 289.
- [24] B.-H. Kim, K. S. Yang, H.-G. Woo, K. Oshida, *Synth. Met.* **2011**, 161, 1211.
- [25] L.-F. Chen, Z.-H. Huang, H.-W. Liang, H.-L. Gao, S.-H. Yu, *Adv. Funct. Mater.* **2014**, 24, 5104.
- [26] B.-H. Kim, C. H. Kim, K. S. Yang, A. Rahy, D. J. Yang, *Electrochim. Acta* **2012**, 83, 335.
- [27] a) O. A. Williams, *Diamond Relat. Mater.* **2011**, 20, 621; b) J. Hees, A. Kriele, O. A. Williams, *Chem. Phys. Lett.* **2011**, 509, 12; c) O. A. Williams, O. Douhéret, M. Daenen, K. Haenen, E. Ōsawa, M. Takahashi, *Chem. Phys. Lett.* **2007**, 445, 255; d) W. Gajewski, P. Achatz, O. A. Williams, K. Haenen, E. Bustarret, M. Stutzmann, J. A. Garrido, *Phys. Rev. B* **2009**, 79, 045206.
- [28] F. Béguin, V. Presser, A. Balducci, E. Frackowiak, *Adv. Mater.* **2014**, 26, 2219.